International Journal of Nanomedicine

Dovepress
open access to scientific and medical research

Open Access Full Text Article

ORIGINAL RESEARCH

ROS-Responsive Nanoprobes for Bimodal Imaging-Guided Cancer Targeted Combinatorial Therapy

Fujie Jiang[1,*], Shuling Liu[1,*], Lu Wang[1], Huifang Chen[1], Yao Huang[2], Ying Cao[2], Xiaoxia Wang[1], Meng Lin[1], Jiuquan Zhang[1]

[1]Department of Radiology, Chongqing University Cancer Hospital, Chongqing Key Laboratory for Intelligent Oncology in Breast Cancer (iCQBC), Chongqing, 400030, People's Republic of China; [2]School of Medicine, Chongqing University, Chongqing, 400030, People's Republic of China

*These authors contributed equally to this work

Correspondence: Jiuquan Zhang; Meng Lin, Department of Radiology Chongqing University Cancer Hospital, No. 181 Hanyu Road, Shapingba District, Chongqing, 400030, People's Republic of China, Tel/Fax +86-23-65079339, Email zhangjq_radiol@foxmail.com; 15823113338@139.com

Purpose: Chemotherapy mediated by Reactive oxygen species (ROS)-responsive drug delivery systems can potentially mitigate the toxic side effects of chemotherapeutic drugs and significantly enhance their therapeutic efficacy. However, achieving precise targeted drug delivery and real-time control of ROS-responsive drug release at tumor sites remains a formidable challenge. Therefore, this study aimed to describe a ROS-responsive drug delivery system with specific tumor targeting capabilities for mitigating chemotherapy-induced toxicity while enhancing therapeutic efficacy under guidance of Fluorescence (FL) and Magnetic resonance (MR) bimodal imaging.

Methods: Indocyanine green (ICG), Doxorubicin (DOX) prodrug pB-DOX and Superparamagnetic iron oxide (SPIO, Fe_3O_4) were encapsulated in poly(lactic-co-glycolic acid) (PLGA) by double emulsification method to prepare ICG/ pB-DOX/ Fe_3O_4/ PLGA nanoparticles (IBFP NPs). The surface of IBFP NPs was functionalized with mammaglobin antibodies (mAbs) by carbodiimide method to construct the breast cancer-targeting mAbs/ IBFP NPs (MIBFP NPs). Thereafter, FL and MR bimodal imaging ability of MIBFP NPs was evaluated in vitro and in vivo. Finally, the combined photodynamic therapy (PDT) and chemotherapy efficacy evaluation based on MIBFP NPs was studied.

Results: The multifunctional MIBFP NPs exhibited significant targeting efficacy for breast cancer. FL and MR bimodal imaging clearly displayed the distribution of the targeting MIBFP NPs in vivo. Upon near-infrared laser irradiation, the MIBFP NPs loaded with ICG effectively generated ROS for PDT, enabling precise tumor ablation. Simultaneously, it triggered activation of the pB-DOX by cleaving its sensitive moiety, thereby restoring DOX activity and achieving ROS-responsive targeted chemotherapy. Furthermore, the MIBFP NPs combined PDT and chemotherapy to enhance the efficiency of tumor ablation under guidance of bimodal imaging.

Conclusion: MIBFP NPs constitute a novel dual-modality imaging-guided drug delivery system for targeted breast cancer therapy and offer precise and controlled combined treatment options.

Keywords: targeted drug delivery, photodynamic therapy, ROS-responsive chemotherapy, bimodal imaging

Introduction

Chemotherapy is the cornerstone of clinical breast cancer treatment. However, its non-specific distribution in the human body often leads to severe systemic toxicity and side effects. Moreover, chemotherapy alone has limited efficacy, resulting in unfavorable outcomes.[1–3] Therefore, there is an urgent need for effective treatment strategies to overcome the challenges associated with therapy of breast cancer. Numerous studies have focused on developing stimulus-responsive drug delivery systems aimed at reducing chemotherapy's side effects while enhancing its effectiveness in the past decade. These innovative drug delivery systems selectively release or activate anticancer drugs in response to internal stimuli present within the tumor microenvironment (TME).[4] For instance, ROS,[5] pH,[6,7] glutathione (GSH)[8] are commonly utilized as internal stimuli triggers. Because both cancer and normal cells have endosomes/lysosomes with acidic pH[9] and high

Received: 6 March 2024
Accepted: 17 July 2024
Published: 7 August 2024

intracellular concentrations of GSH ($2 * 10^{-3}$ to $10 * 10^{-3}$ M),[10] the widely reported pH- and GSH- based responsive drug delivery systems offer limited selectivity. In contrast, cancer cells exhibited elevated levels of ROS including hydroxyl radicals (OH·) and hydrogen peroxide (H_2O_2) in comparison to normal cells.[11] Therefore, ROS-responsive drug delivery systems offer greater selectivity in releasing drugs specifically within cancer cells. Currently available drug delivery systems employ ROS responsive polymers like polythioether ketal,[12] and selenium-containing copolymers.[13] Those systems generally release encapsulated drug based on a phase change induced carrier disassembly and they have increased ROS sensitivity with increasing electronegativity. Polymers containing diselenides and oxalate are usually degraded into small pieces to release the cargo.[14] However, their efficiency remains suboptimal due to inherent heterogeneity within tumors themselves which limits selective activation of released drugs leading to compromised anticancer efficacy and increased side effects. Consequently, exogenous mediators need be introduced into these systems aiming at enhancing production of ROS thereby activating reactive drugs more effectively thus improving overall therapeutic outcome.

Increasing the concentration of ROS at the target site through external stimuli such as laser[15,16] and ultrasound,[17] a more effective triggering of drug release can be achieved. In recent years, PDT has garnered significant attention due to its potential advantages in terms of noninvasiveness, controllability, and high precision. PDT is a promising approach for cancer treatment that involves inducing excessive ROS production by irradiating photosensitive photosensitizers (PSs) with laser light. The cytotoxicity of the generated ROS selectively affects tumor cells while protecting normal tissues from damage caused by light irradiation.[18] ICG, which is a commonly used photosensitizer, produces abundant ROS under 808 nm laser irradiation, enabling effective tumor cell killing through PDT. Additionally, ICG exhibits remarkable near-infrared absorption capacity that facilitates FL imaging of tumor sites. The ROS generated during PDT can directly induce cancer cell death via necrosis or apoptosis and activate tumor-specific chemotherapy prodrugs. The advent of chemotherapy prodrugs brings new hope for solid tumors as they are chemically modified compounds that remain inactive in vitro but convert into biologically active components in vivo upon administration.[19] Through rational design approaches involving various chemotherapy prodrugs such as DOX[20] and PTX,[21] the delivery efficiency of anticancer drugs can be significantly enhanced while minimizing damage to surrounding normal tissues. A synergistic strategy was employed to achieve efficient co-delivery of the photosensitizer and the ROS-responsive DOX prodrug pB DOX[22,23] using 808 nm laser irradiation for achieving targeted killing effects on tumor tissues while reducing off-target toxicity.[24]

The accumulation of responsive drug delivery in tumors is crucial for enhancing therapeutic efficacy. However, conventional responsive drug delivery systems are designed with stealthy surface materials to achieve prolonged blood circulation time.[25] These systems utilize the enhanced permeability and retention effect resulting from tumor vascular system leakage to selectively release anticancer active drugs.[26] Nevertheless, the heterogeneous nature and complex microenvironment of tumors significantly reduce the delivery capacity of nanosystems, leading to insufficient retention of responsive prodrugs within tumors and consequently impacting therapeutic efficacy and safety.[27,28] Ligands can target overexpressed receptors on tumor cells, enabling effective active targeting performance when coupled with nanodrugs. Incorporating active targeting ligands onto the surface of nanosystems improves their specificity towards tumor cells rather than healthy cells.[29] Therefore, targeted coupling of antibodies and ligands presents a novel approach for precision targeted therapy in breast cancer research. Mammaglobin A (Mam-A) exhibits high specificity for breast cancer and is upregulated in various genotypes including luminal A and triple negative breast cancer.[30–32] Consequently, Mam-A represents a promising molecular target for breast cancer treatment.[33] The mammaglobin-targeting monoclonal antibodies (mAbs) selectively binds to ZR75.1 breast cancer cells that overexpress Mam-A on their surface. Combining this monoclonal antibody with a nanoplatform enables efficient penetration through the bloodstream while significantly increasing drug accumulation at the site of breast tumors, thereby enhancing drug delivery capabilities.[34]

Multimodal imaging guided ROS-responsive systems need to be introduced to ensure accurate breast cancer therapy.[35] Each imaging technique has its inherent limitations, however, such as the relatively low sensitivity of MR imaging and the insufficient penetration into the deep tissue of FL imaging. Therefore, developing novel imaging contrast agent that integrate the distinct strengths of different imaging techniques would be valuable for biomedical diagnosis.[36] Bimodal imaging provides more detailed diagnostic information than unimodal imaging.[37,38] FL imaging guided by PSs and T2 weight MR imaging guided by the Fe_3O_4 NPs can accurately assess the therapeutic effect of ROS responsive chemotherapy. Furthermore, accurate tumor diagnosis can improve the rate of prognosis and survival. Therefore,

combining FL and MR imaging is significantly important in breast cancer diagnosis and effectively compensating for limitations associated with single imaging.[39,40]

These studies have demonstrated that the integration of nano-responsive delivery systems and targeted antibody-ligand therapy can enhance the efficacy and safety of tumor treatment. Therefore, this study aims to construct and develop a novel drug delivery system comprising mAbs specifically targeting breast cancer and multifunctional responsive NPs. As shown in Scheme 1, A functional poly (lactic-co-glycolic acid) (PLGA) nanosystems was prepared, incorporating ROS-responsive prodrug pB-DOX, photosensitizer ICG, and T2-weighted MR imaging contrast agent Fe_3O_4 (ICG/pB-DOX/ Fe_3O_4/PLGA NPs, IBFP NPs). Subsequently, mAbs with targeting ability were conjugated onto the surface of the nanosystems (mAbs/ICG/pB-DOX/ Fe_3O_4/PLGA NPs, MIBFP NPs) to facilitate dual-modal imaging as well as synergistic ROS-responsive PDT and chemotherapy for tumor treatment. Upon injection into the body, the multifunctional targeted nanosystems exhibited specific retention in tumors due to mAbs' targeting capability. Under near-infrared laser irradiation, the retained nanosystems containing ICG generated ROS for PDT therapy while simultaneously cleaving sensitive bonds of pB-DOX to restore DOX activity. Finally, guided by FL and MR dual-modal imaging, targeted therapy combining PDT with chemotherapy was performed for tumors. In summary, we have developed a novel approach enabling effective drug release at tumor sites while providing a safe and efficient candidate for synergistic tumor treatment.

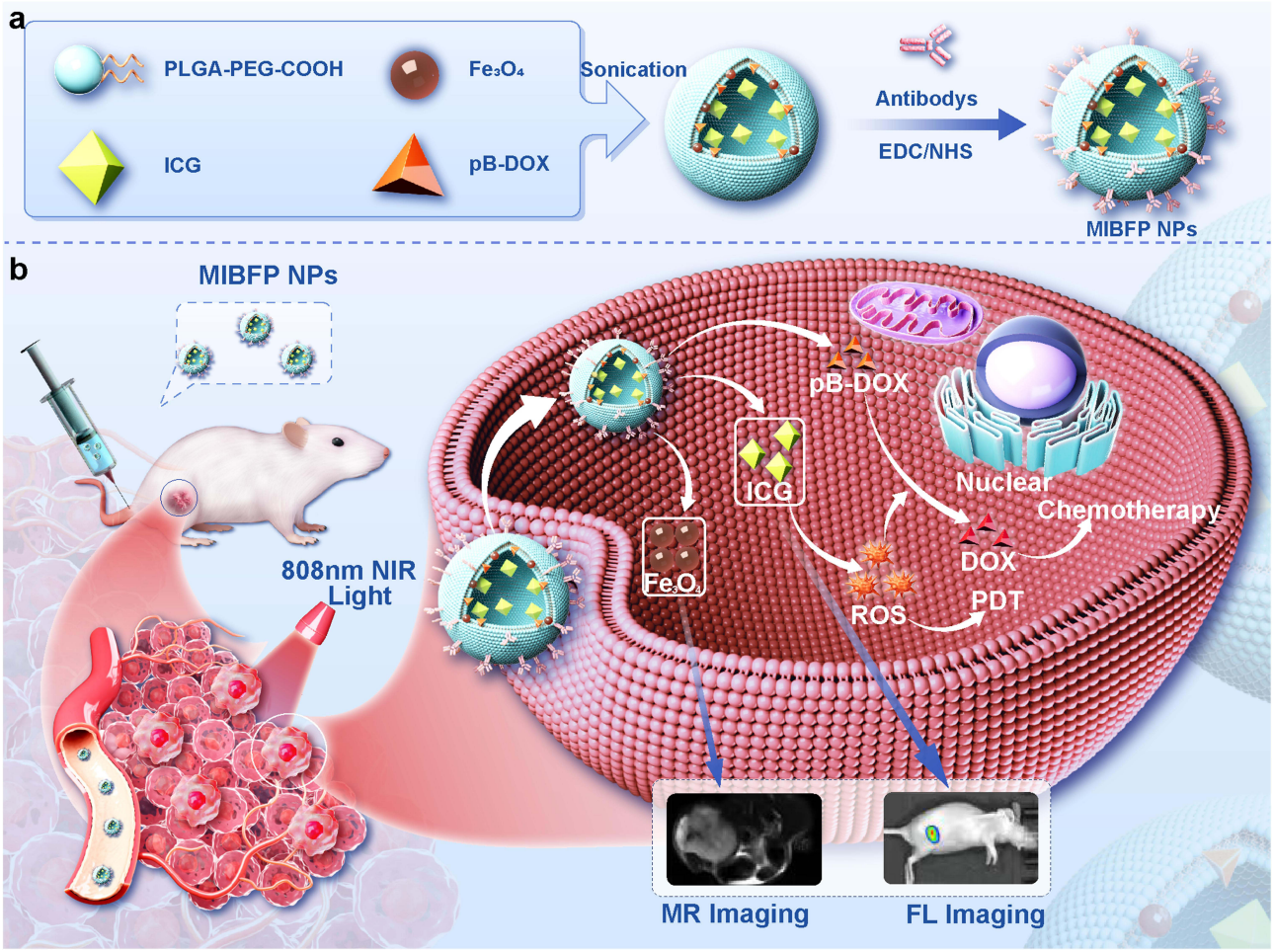

Scheme 1 a) Schematic illustration of MIBFP NPs synthesis. **b)** Schematic illustration of the synergistic effect of the MIBFP NPs combined with PDT and ROS-responsive chemotherapy on cancer cells. (1) ICG-generated ROS PDT induces cell necrosis or apoptosis and selectively leaves the boronate moiety of pB-DOX under 808 nm laser irradiation, triggering DOX release for chemotherapy. (2) MIBFP NPs offer FL and MR imaging approaches for visualizing their dynamic distribution within the whole body. **Abbreviations:** mAbs, mammaglobin antibodys; ICG, indocyanine green; pB-DOX, doxorubicin prodrug; Fe_3O_4, superparamagnetic iron oxide; MIBFP NPs, mAbs, ICG, pB-DOX and Fe_3O_4, coloaded poly (lactic-co-glycolic acid) nanoparticles; PDT, photodynamic therapy; ROS, Reactive oxygen species; FL, fluorescence; MR, magnetic resonance.

Materials and Methods

Materials

Polyethylene glycol (PEG), poly (lactic-co-glycolic acid) (PLGA) (50:50, MW=13,000) and PLGA-PEG-COOH were purchased from Jinan Daigang Biomaterial Co., Ltd (ShanDong, China). Fe_3O_4 iron oxide NPs (10 nm, 25 mg mL^{-1}) were obtained from Ocean Nanotech Co., Ltd. (San Diego, CA, USA). ICG was obtained from MedChemExpress (New Jersey, USA). pB-DOX was purchased from Xi'an Haoran Biotechnology Co., Ltd (Shanxi, China). Mam-A mAbs and fluorescein isothiocyanate (FITC)- mAbs were purchased from Thermo Fisher Scientific (Waltham, MA, USA). 1,3-Diphenylisobenzofuran (DPBF), 2′,7′-dichlorofluorescin diacetate (DCFH-DA), and 4,6-diamidino-2-phenylindole (DAPI) were obtained from Beyotime Biotechnology Ltd., Co. (Shanghai, China). 1-Ethyl-3-(3-dimethylaminopropyl) carbodiimide hydrochloride (EDC), N-hydroxysulfosuccinimide (sulfo-NHS), MES buffer and poly (vinyl alcohol) (PVA, MW=25,000) were purchased from Sigma-Aldrich Chemical Co. (St Louis, MO, USA). The Cell Counting Kit-8 (CCK-8), Hoechst 33,324, and calcein-AM/PI double staining kits were obtained from Dojindo Laboratories (Kumamoto, Japan). All other chemicals used were of analytical grade and were used directly without further purification.

Fabrication of the NPs

IBFP NPs were prepared using a double emulsion method.[41] First, 100 mg of PLGA, 3 mg of pB-DOX, and 200 μL of Fe_3O_4 were added to 2 mL of chloroform ($CHCl_3$) and stirred to produce a homogeneous mixture. Then, 3.5 mg of ICG aqueous solution was added, and the mixture was emulsified using an ultrasonic emulsion breaker (SCIENTZ-IID, Xinzhi Biotechnology, Zhejiang) at 120 W for 5 min to obtain the primary emulsion. Subsequently, 4 mL of precooled 4% PVA solution was added to the primary emulsion, which was emulsified again by an ultrasonic crusher to obtain the W/O/W double emulsion. Then 10 mL of 2% isopropanol was added, and the mixture was mechanically stirred for 6 h. The emulsion was centrifuged at 10,000 rpm for 5 min and subsequently purified by squeezing 10 times using a 200 nm polycarbonate filter, after which the resulting IBFP NPs were stored at 4°C. The PLGA/pB-DOX NPs (BP NPs), PLGA/ICG NPs (IP NPs), PLGA/ICG/pB-DOX NPs (IBP NPs), PLGA/Fe_3O_4 NPs (FP NPs), and PLGA/pB-DOX/Fe_3O_4 NPs (BFP NPs) were prepared in the same manner.

The mAbs and IBFP NPs were linked using the carbodiimide method. First, appropriate IBFP NPs were dispersed in 0.1 M MES buffer solution (pH = 5.2), and EDC and NHS at a mass ratio of 2: 1 were added to activate the carboxyl terminus of the IBFP NPs, and the reaction lasted for 2 h. The unreacted EDC and NHS were removed by centrifugation at 1000 rpm for 5 min. Then, the activated IBFP NPs and excess mAbs were dispersed in 0.1 M MES buffer solution (pH = 8). After mixing, the mixture was placed on a shaking table and reacted for 12 h. Finally, the mAb-IBFP NPs (MIBFP NPs) were obtained by centrifugation at 1000 rpm for 5 min. The mAb-PLGA/pB-DOX NPs (MBP NPs), mAb-PLGA/ICG NPs (MIP NPs), mAb-PLGA/ICG/pB-DOX NPs (MIBP NPs), and mAb-PLGA/pB-DOX/Fe_3O_4 NPs (MBFP NPs) were similarly generated.

Characterization of the NPs

The size distributions, zeta potentials, and polydispersity indices (PDIs) of the NPs were measured using a Malvern Zeta Sizer Nano Series instrument (NanoBrook Omni, Brookhaven, USA), and the morphology and structure were observed via transmission electron microscopy (TEM, Talos F200S, Thermo Fisher Scientific, NL). To investigate the stability of the MIBFP NPs, the zeta potential and size were tested at different time points (1, 3, 5, 7, and 9 days) in phosphate-buffered solution (PBS) and 10% fetal bovine serum (FBS). The above formulations were monitored using UV–vis-NIR spectroscopy (UV-3600, Shimadzu, Japan). After ultrafiltration centrifugation and organic solvent extraction, the encapsulation efficiencies (EEs) of pB-DOX and ICG in the PLGA NPs were quantified and calculated using HPLC and UV–vis-NIR spectroscopy, respectively. UV–vis-NIR absorption at 780 nm was used to determine the ICG concentration. The Fe content was tested using inductively coupled plasma–optical emission spectrometry (ICP–OES 5110, Agilent Co. Ltd., USA). FITC-mAb-conjugated IBFP NPs were observed under a confocal laser scanning microscope (CLSM, LAS X, Leica, Germany) to further confirm the coupling of the mAbs to the IBFP NPs. The carrier rate of the mAbs was analyzed using flow cytometry (FCM, NovoExpress, Agilent, USA). The experimental details of the Biocompatibility and biosafety evaluation can be found in Supporting Information 1.

Cell Culture

The human breast cancer cell line ZR75-1, Human Mammary Epithelial Cells (HMECs) and vascular smooth muscle cells (VSMCs) were obtained from the Chinese Academy of Sciences. All cells were cultured in Roswell Park Memorial Institute-1640 (RPMI-1640) medium supplemented with 1% penicillin/streptomycin and 10% FBS and incubated in a 5% CO_2 atmosphere at 37°C.

Animal Models

All female BALB/c nude mice (6–8 weeks old) were purchased from Beijing Vital River Laboratory Animal Technology Co., Ltd. All the protocols for the animal experiments were approved by the Animal Ethics Committee of the Chongqing University Cancer Hospital and conducted in strict accordance with the guidelines of the Institutional Animal Care and Use Committee of China. Female BALB/c nude mice were subcutaneously injected in the right flank with 1×10^6 ZR75.1 cells suspended in 100 μL of PBS. Generally, tumors were palpable within 14 days. Tumor volume was calculated using the following formula: (length × width^2) 2^{-1}.

Cellular Uptake

ZR75.1 cells were cultured via CLSM for 24 h, followed by the addition of an MIBFP NP (pB-DOX, 6.0 μg mL^{-1}) solution and further incubation for 12 h. After washing three times with PBS, the cells were successively incubated with Hoechst 33,334 for 15 min. Subsequently, the cells were washed three times before being observed via CLSM. For the quantitative assessment of intracellular uptake, ZR75.1 cells were seeded into six-well plates, incubated with the MIBFP NPs for 12 h, washed with PBS, and analyzed using FCM. The experimental details of the ZR75.1 and HMEC cellular uptake for different durations (2 h and 12 h) can be found in Supporting Information 1.2.

To further compare the targeting ability of the different NPs, ZR75.1 cells were divided into five groups: the PBS control, BFP NP, IBFP NP, MBFP NP, and MIBFP NP groups. The corresponding culture dishes were supplemented with different dilutions of NPs (pB-DOX at a concentration of 6.0 μg mL^{-1}). The FL intensity was quantified using inverted FCM. To study the effect of ROS on the activity recovery of pB-DOX, the cells were exposed to 808 nm irradiation (1 W cm^{-2}) for different time periods (0 min, 1 min and 2 min) after MIBFP NPs incubation for 12 h, and the FL intensity was determined by FCM.

Singlet Oxygen ($^1O_2$) Detection

The $^1O_2$ generation ability of the MIBFP NPs was evaluated in vitro by DPBF.[42] The MIBFP NPs (15 μg mL^{-1} ICG, 3 mL) were rapidly mixed with fresh DPBF (0.5 mg mL^{-1}, 100 μL) and stored in the dark. Subsequently, the mixture was irradiated using an 808 nm laser (1 W cm^{-2}) for different durations (0, 20, 40, 60, and 80s). Finally, the absorbance was measured at a wavelength of 410 nm using a UV–vis-NIR spectrophotometer. Then, $^1O_2$ production after 808 nm laser irradiation (1 W cm^{-2}, 1 min) of the MIBFP NPs at different concentrations (0, 20, 40, 60, and 80 μg mL^{-1}) was measured. The ability to generate ROS was evaluated by observing the changes in the UV absorption of DPBF at 410 nm.

Intracellular ROS Detection

The intracellular production of ROS was assessed using DCFH-DA. ZR75.1 cells were seeded in 12-well plates at a density of 2×10^5 cells per well for 12 h, followed by treatment with fresh media containing 1 mL of PBS, MBP NPs, MIP NPs, or MIBFP NPs (for which the ICG concentration was 5 μg mL^{-1}). The cells were then further incubated at 37°C and 5% CO_2 for 2 h. After washing with PBS three times, the cells were cultured with 1 mL of DCFH-DA (25 μM) for 20 min. Subsequently, the cells were irradiated with an intensity of 1.0 W cm^{-2} from an 808 nm laser, stained with Hoechst 33258 and observed by CLSM. The FL intensity was quantitatively analyzed using FCM.

In vitro Cytotoxicity

The cytotoxicity of combination therapy on ZR 75.1 cells under different disposes were assessed using CCK-8 assay. First, ZR 75.1 cells (1 * 10^4 cells per well) were incubated in 96-well plates for 24 h. Then, the cells treated with DOX,

MBP NPs, MIP NPs + laser and MIBFP NPs + laser at different concentrations in media. During incubation, laser irradiation was given (808 nm at 1 W cm^{-2}). After 24 h, the cells were further incubated with CCK-8 solution for 4 h. Finally, the absorption of each well was measured using a microplate reader.

ZR75.1 cells were seeded in a confocal dish to investigate the synergistic effect of PDT and chemotherapy using the MIBFP NPs. After 24 h, the cells were treated with PBS, MBP NPs, MIP NPs, MIBFP NPs, PBS + laser, MBP NPs + laser, MIP NPs + laser, or MIBFP NPs + laser. Subsequently, the ZR75.1 cells were irradiated with a laser (808 nm at 1 W cm^{-2}). According to the instructions provided by the kit manufacturer's protocol, live cells were stained with calcein-acetoxymethyl (AM), while dead cells were stained with propyl iodide (PI). The samples were then observed using CLSM. Finally, Image J software was used to calculate the ratio of viable to nonviable cells.

In vitro and in vivo Bimodal Imaging

FL Imaging and Biodistribution

The FL imaging characteristics of the MIBFP NPs were observed using an IVIS Spectrum imaging system (IVIS Lumina III; PerkinElmer, Waltham, MA, USA) with excitation at a wavelength of 745 nm and detection through an 820 nm filter. Various concentrations of NPs (ICG ranging from 1.0 to 200 μg mL^{-1}) were added to a 96-well plate for FL image acquisition, followed by analysis using the FL analysis system to determine the corresponding FL signals. For in vivo FL imaging, the MIBFP NPs (ICG: 3.5 mg kg^{-1}) were intravenously administered to ZR75.1 tumor-bearing mice.[43,44] Subsequently, FL images were acquired at different time points post-injection (pre, 1, 6, 12, and 24 h). At 24 h after injection, the major organs (heart, liver, spleen, lung, and kidney) and tumor tissues were collected for ex vivo FL imaging to determine the biodistribution of the MIBFP NPs.

MR Imaging

The MR imaging experiments were conducted using a clinical MRI system (MAGNETOM Prisma 3.0T, Siemens Ltd., Germany) equipped with a specialized small animal coil (Medcoil, Zhongzhi Medical Ltd., China). The MRI parameters were as follows: fast field echo, TR = 650.0 ms, TE = 11 ms, and slice thickness = 1.4 mm. The MIBFP NPs were diluted to the specified concentrations (Fe concentrations: 0, 0.0625, 0.125, 0.25, 0.5, and 0.625 mM). Subsequently, the samples were transferred into Eppendorf tubes with a capacity of 2 mL for T2-weighted MRI analysis to measure the corresponding T2 relaxation time within the region of interest (ROI) and calculate the T2 relaxation coefficient (r1). To investigate T2-weighted MR imaging in vivo, ZR75.1 tumor-bearing mice were intravenously injected with MIBFP NP solution (2 mg mL^{-1}, 200 μL), and MR images of tumor sites were captured at different time points (pre, 1, 6, 12, and 24 h). The T2 SI in the tumor region (SI tumor) was measured. The percentage of signal intensity decrease (PSID) was used to assess the MRI effectiveness, PSID = (SI pre − SI post)/SI pre × 100%.

In vivo Antitumor Efficiency

When the tumor volume reached 150–200 mm^3, the ZR75.1 tumor-bearing mice were randomly divided into eight groups (n = 5): (1) PBS, (2) laser only, (3) MIBP NPs, (4) MIBFP NPs, (5) MIP NPs + laser, (6) MIBP NPs + laser, (7) IBFP NPs + laser, and (8) MIBFP NPs + laser (DOX equivalent of 3.0 mg kg^{-1}, ICG of 3.5 mg kg^{-1}). Treatment was administered via intravenous injection followed by irradiation of the laser group using a power intensity of 1 W cm^{-2} for 2 min after a 12 h interval post-injection. Tumor volume and weight were measured every 3 days for 15 days using the following formula: tumor volume = length × $(width)^2$ 2^{-1}. The average tumor volume after treatment was used to plot the tumor growth curve and assess the weight of the tumor-bearing mice. On day 15, the mice of each group were sacrificed to obtain the tumor. And the tumors were subsequently fixed in formalin and embedded in paraffin for hematoxylin and eosin staining (H&E), Terminal-deoxynucleotidyl Transferase Mediated Nick End Labeling (TUNEL), and Proliferating cell nuclear antigen (PCNA) staining. The experimental details of H&E staining of major organs after antitumor therapy can be found in Supporting Information 1.3.

Statistical Analysis

All statistical analyses were performed using GraphPad Prism 8 software (San Diego, CA, USA). The data are expressed as the mean ± standard deviation. Significance was evaluated using Student's *t*-test and one-way ANOVA. P values < 0.05 were considered to indicate significance (NS, not significant; $*P < 0.05$, $**P < 0.01$, $***P < 0.001$, and $****P < 0.0001$).

Results and Discussion

Synthesis and Characterization of MIBFP NPs

We encapsulated ICG, pB-DOX, and Fe_3O_4 in PLGA and successfully linked the mAbs to synthesize the MIBFP NPs. TEM and DLS images showed that the MIBFP NPs had a well-defined spherical shape and uniform size. TEM images showed that Fe_3O_4 was uniformly distributed in the MIBFP NPs (Figure 1a). TEM energy dispersive spectroscopy (EDS) line scans showed that the MIBFP NPs contained C, N, O, Fe, and B (Figure 1b). DLS measurements revealed that the average hydrodynamic diameter of the MIBFP NPs was approximately 180.55 ± 3.38 nm, the PDI was 0.07 ± 0.03

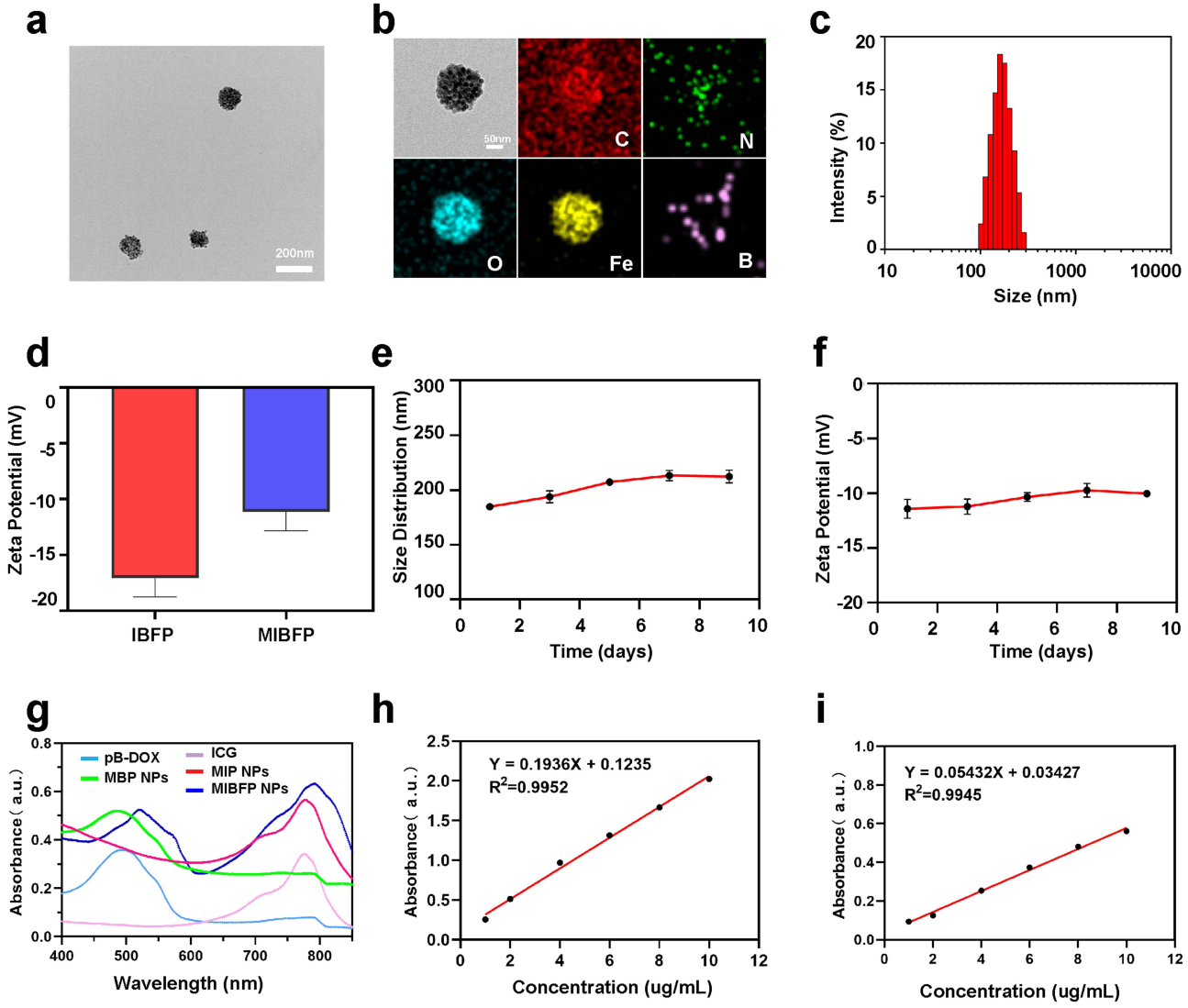

Figure 1 Synthesis and characterization of MIBFP NPs. (**a**) TEM image and (**b**) TEM EDS line scans image of MIBFP NPs, (**c**) Size distribution analysis of MIBFP NPs, (**d**) Zeta potentials comparison between MIBFP and IBFP NPs, (**e**) Time-dependent particle size changes of MIBFP NPs within 9 days, (**f**) Zeta potential evolution of MIBFP NPs within 9 days, (**g**) UV-vis-NIR absorption spectra comparison among pB-DOX, MBP NPs, ICG, MIP NPs and MIBFP NPs. (**h**) Relative absorbance measurement at 780 nm wavelength for different concentrations of ICG. (**i**) The relative absorbance measurement at 480 nm wavelength for different concentrations of pB-DOX.

Abbreviations: mAbs, mammaglobin antibodies; ICG, indocyanine green; pB-DOX, doxorubicin prodrug; Fe_3O_4, superparamagnetic iron oxide; MIBFP NPs, mAbs, ICG, pB-DOX and Fe_3O_4, coloaded poly (lactic-co-glycolic acid) nanoparticles; TEM, transmission electron microscopy; EDS, energy dispersive spectroscopy.

(Figure 1c), and the average zeta potential was −17.07 ± 1.67 mV, which increased to −11.13 ± 1.71 mV after the conjugation of the mAbs (Figure 1d), indicating successful conjugation. During the 9-day monitoring period, no significant change occurred in the average size or zeta potential of the MIBFP NPs (Figure 1e and f), demonstrating that the MIBFP NPs had excellent stability under physiological conditions. The UV–vis-NIR spectra of the MIBFP NPs and MIP NPs exhibited the characteristic absorption peak of ICG at 780 nm and the characteristic absorption peak of pB-DOX at 480 nm for the MIBFP NPs and MBP NPs (Figure 1g), confirming the successful loading of ICG and pB-DOX. The slight red shift in the absorption spectra of the IP NPs and MIBFP NPs from 780 nm to 815 nm may be due to the tight alignment of ICG in the PLGA NPs or the addition of pB-DOX, which is absorbed at longer wavelengths than a single ICG molecule. UV–vis-NIR spectrophotometric measurements revealed that the absorbance of ICG at 780 nm was linearly related to the concentration (Figure 1h), and the absorbance of pB-DOX at 480 nm also showed an excellent linear relationship (Figure 1i).

The EEs of ICG in the MIP NPs and MIBFP NPs were calculated to be 80.72 ± 7.02% and 61.43 ± 3.32%, respectively. The entrapment efficiencies of pB-DOX in the MBP NPs and MIBFP NPs were calculated to be 82.96 ± 8.16% and 56.01 ± 4.58%, respectively. The entrapment efficiencies of Fe_3O_4 in the MFP NPs and MIBFP NPs were calculated to be 79.64 ± 1.66% and 40.80 ± 0.87%, respectively. These results indicate that when ICG, pB-DOX, and Fe_3O_4 are loaded simultaneously, the EEs of both will decrease.

CLSM confirmed the covalent coupling of the mAbs and MIBFP NPs. The green fluorescent mAbs overlapped with the red fluorescent MIBFP NPs, as indicated by yellow FL, confirming the successful binding of the mAbs to the MIBFP NPs (Figure 2a). Moreover, the FCM results showed that the binding rate of the mAbs to the MIBFP NPs was as high as 80.36 ± 2.77% (Figure 2b). The abovementioned findings indicate that the mAbs were successfully coupled to the surface of the MIBFP NPs, providing the necessary conditions for the effective and specific targeting of breast cancer cells. Passive targeting is mostly achievable during diffusion-mediated transport. A size range of 40–200 nm is considered to be most favorable for an extended circulation time and augmented buildup inside the tumor mass.[45] Passive targeting by NPs occurs because of the uniqueness of solid tumors by enhanced permeability and retention (EPR) effect.[46] However, premature drug release is a major concern for such passive targeting. Recently, active targeting means modifying the surface of NPs using the targeting ligands to precisely direct to the specific receptors overexpressed on tumor cells. The targeted ligands include antibodies, polysaccharides, and proteins, among others.[47] In this study, we mainly constructed the active targeting NPs by binding with specific targeting mAbs of breast cancer cells to overcome the obstacle of drug delivery and enhance the accumulation of NPs in tumor.

We assessed the cytotoxicity of the MIBFP NPs on ZR75.1 and VMSCs. Remarkably, even at a high concentration of 15 μg mL-1 ICG, the cell survival rate remained above 85%, indicating that all the NPs had negligible effects on the viability of the ZR75.1 (Figure S1) and VMSCs cells (Figure S2). No significant differences were observed in blood parameters or whole blood cell counts among the experimental groups (Figure S3). Histopathological examination (H&E) staining revealed no notable damage to major organs in any group (Figure S4). These findings indicate that the MIBFP NPs exhibit high biocompatibility and biological safety in vitro and in vivo.

Cellular Uptake

The effective accumulation of PSs in tumor tissue is a prerequisite for PDT. CLSM was further used to observe the subcellular drug distribution and release in cells treated with BFP NPs, IBFP NPs, MBFP NPs and MIBFP NPs. The red FL intensity of pB-DOX was mainly distributed in the cytoplasm after 2 h incubation with MIBFP NPs. A strong nuclear FL intensity was observed after 12 h incubation (Figure S5). Subsequently, we compared the endocytosis of different NPs by ZR75.1 cells after 12 h incubation. The MIBFP NPs had the greatest cellular uptake, followed by the BFP NPs, IBFP NPs, and MBFP NPs (Figure 3a). Moreover, the FCM results also demonstrated the highest FL intensity in the MIBFP NP group (Figure 3b), this is because mAbs conjugated NPs will enhance the intracellular retention indicating that the mAbs effectively facilitated NPs uptake by ZR75.1 cells. In contrast, MIBFP NPs does not show targeting cellular uptake to the normal HMEC cells (Figure S6). The localization of DOX or pB-DOX within the nucleus is crucial for inducing apoptosis, as DOX or pB-DOX exerts its action on DNA and topoisomerase II, both of which are predominantly located in this cellular compartment.

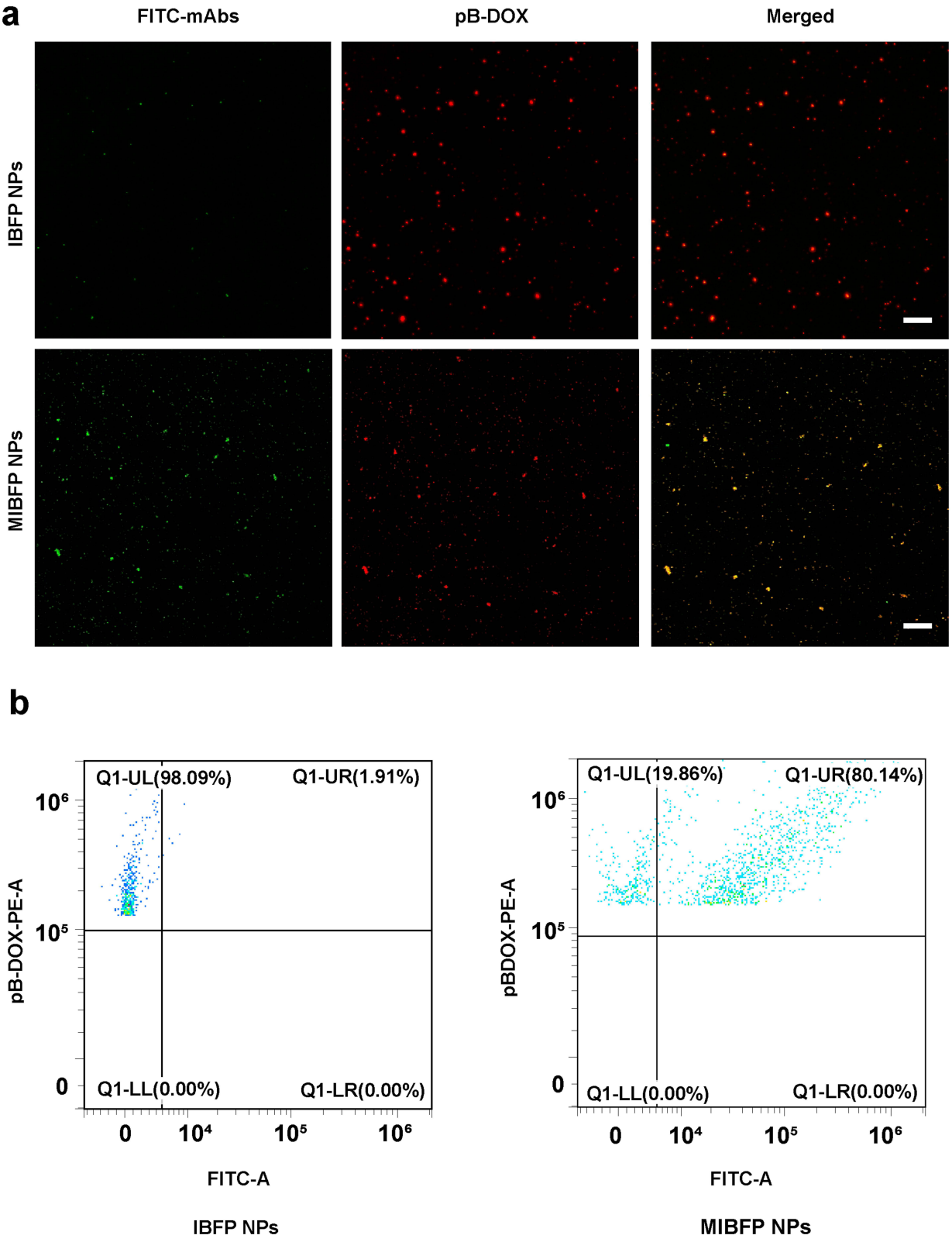

Figure 2 In vitro construction of the mAbs targeting NPs. (**a**) CLSM images analysis binding between FITC-labeled mAbs and IBFP NPs. (**b**) Flow cytometry analysis binding between mAbs and IBFP NPs.

Abbreviations: mAbs, mammaglobin antibodies; NPs, nanoparticles; IBFP NPs, ICG, pB-DOX and Fe_3O_4, coloaded poly (lactic-co-glycolic acid) nanoparticles; CLSM, confocal laser scanning microscope; FITC, fluorescein isothiocyanate.

https://doi.org/10.2147/IJN.S467512 DovePress

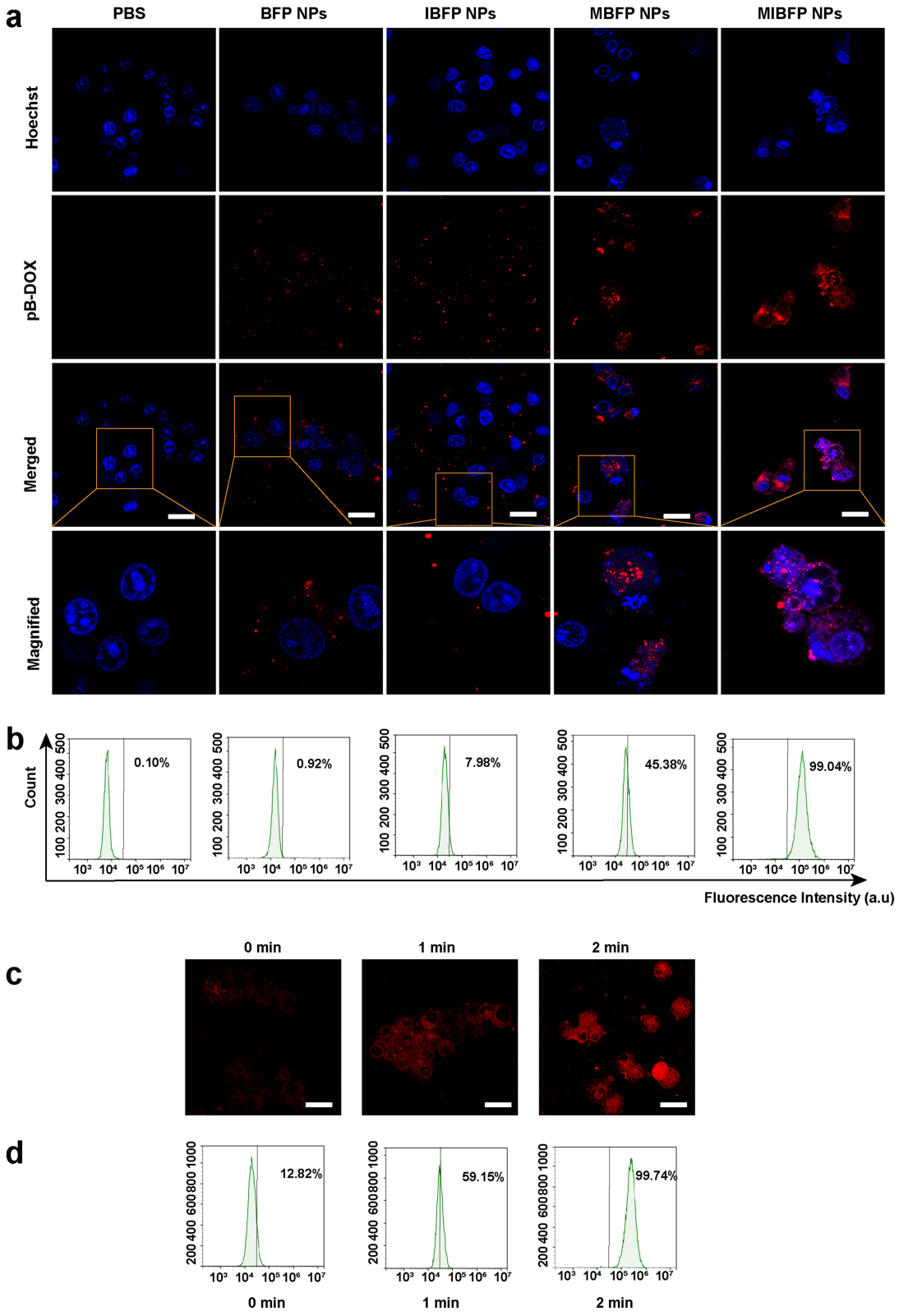

Figure 3 The cellular uptake of the MIBFP NPs for ZR75.1 cells. (**a**) CLSM images of ZR75.1 cells incubated with PBS, BFP NPs, IBFP NPs, MBFP NPs and MIBFP NPs for 12 h. The scale bar is 25 μm. (**b**) FCM analysis of ZR75.1 cells incubated with different treatment groups. (**c**) CLSM images of ZR75.1 cells incubated with MIBFP NPs and irradiated for different incubation periods. The scale bar is 25 μm. (**d**) Flow cytometry analysis of ZR75.1 cells incubated with MIBFP NPs and irradiated for different incubation periods. (Ex: 505 nm / Em: 550 nm for pB-DOX).

Abbreviations: pB-DOX, doxorubicin prodrug; MIBFP NPs, mAbs, ICG, pB-DOX and Fe_3O_4, coloaded poly (lactic-co-glycolic acid) nanoparticles; CLSM, confocal laser scanning microscope; PBS, phosphate-buffered solution; FCM, flow cytometry.

The FL of DOX, which sharply decreased upon conversion into the prodrug pB-DOX, could be recovered once pB-DOX is transformed into DOX. To further validate that sufficient ROS generated by ICG-induced intracellular DOX activation, ZR75.1 cells were incubated with the MIBFP NPs and subsequently irradiated (808 nm, 1 W cm^{-2}) for 0 min, 1 min and 2 min while monitoring changes in the intracellular DOX FL intensity. Upon irradiation, the FL intensity of pB-DOX significantly increased and was positively correlated with an increasing irradiation time (Figure 3c and d). Chemotherapy is often unsatisfactory, this is because the presence of multidrug resistance (MDR), which causes chemotherapeutic drugs to be expelled from cancer cells. It is feasible that drug resistance induced by one therapy might be reversed by another therapy.[48] Consequently, several novel treatment strategies, such as PDT, have been developed to enhance MDR cancer treatment. Recently, it has been verified that ROS produced by PSs can cause the photodestruction of ATP-binding cassette (ABC) transporter proteins. The decreased expression of ABC transporter protein will inhibit the efflux of chemotherapeutic and enhance the accumulation of drug in cytosol, which can achieve a synergistic efficiency in chemotherapy.[49,50]

In vitro $^1O_2$ Detection from NPs

The level of $^1O_2$ production plays a crucial role in PDT. The ability of the MIBFP NPs to generate $^1O_2$ via laser irradiation was assessed using the $^1O_2$ probe DPBF. To evaluate the potential of the MIBFP NPs as PSs, we utilized the $^1O_2$ level index DPBF to assess the $^1O_2$ generation capacity of the MIBFP NPs upon 808 nm laser irradiation. The absorption of DPBF exhibited a time-dependent decrease after various durations of 808 nm laser exposure (Figure 4a). Furthermore, the absorption decreased with increasing MIBFP NP concentrations (Figure 4b). Because the decay rate of DPBF was proportional to the rate of $^1O_2$ generation, it was suggested that the MIBFP NPs produced a large volume of $^1O_2$, which played an excellent role in PDT and subsequently activated pB-DOX.

Intracellular ROS Detection

Inspired by the robust ROS production capabilities of the MIBFP NPs, we employed DCFH-DA as a molecular probe for intracellular ROS detection to further explore the potential of the MIBFP NPs (ICG concentration, 15.0 μg mL^{-1}) to generate ROS under 808 nm laser irradiation. CLSM revealed evident green FL in the MIP NPs + Laser and MIBFP NPs + Laser groups (Figure 4c). Upon laser irradiation, the MIBFP NPs produced additional high levels of ROS, enabling their involvement in PDT through near-infrared light and indicating their potential for producing phototherapeutic effects. The PBS, MBP NPs and PBS + Laser groups exhibited negligible green FL, indicating that both the laser and the PSs played indispensable roles in ROS production. Similar quantitative results were obtained using FCM (Figure 4d).

Cellular Cytotoxicity Studies

CCK-8 assay was carried out to quantitatively estimate the cytotoxicity of MIBFP NPs with different concentrations of pB-DOX (Figure 5a). ZR 75.1 cells were treated with DOX, MBP NPS, MIP NPs + Laser and MIBFP NPs + Laser. The cell viabilities decreased with increasing concentration of pB-DOX. The half maximal inhibitory concentration (IC_{50}) values of DOX, MBP NPS, MIP NPs + Laser and MIBFP NPs + Laser were 14.8, 28.0, 75.3 and 4.7 μg/mL (calculated from the pB-DOX concentration), respectively. The results show that MIBFP NPs + Laser has the most optimal efficiency to damage cancer cells compared to other groups.

The ability of the MIBFP NPs to enhance PDT and chemotherapy in vitro was investigated. In the absence of the 808 nm laser, the groups treated with PBS, MBP NPs, MIP NPs, or MIBFP NPs were characterized by green FL, indicating that these NPs had negligible antitumor effects. Similarly, the red FL emitted by the 808 nm laser can be disregarded, confirming the safety of our chosen laser intensity. No significant red FL was observed in the MBP NPs + Laser group, while noticeable red FL was observed in the MIP NPs + Laser group, suggesting that ICG is a crucial factor for PDT activation and that cell killing cannot be achieved without light-activated pB-DOX. The level of red FL was significantly greater in the MIBFP NPs + Laser group than in the MIP NPs + Laser group, which may be attributable to ROS production by internalized ICG upon light exposure leading to the activation of pB-DOX into DOX, synergistically enabling PDT and chemotherapy -induced cell death (Figure 5b and c). These results suggest that the MIBFP NPs possess excellent PDT and chemotherapy effects on cancer cells after 808 nm laser irradiation.

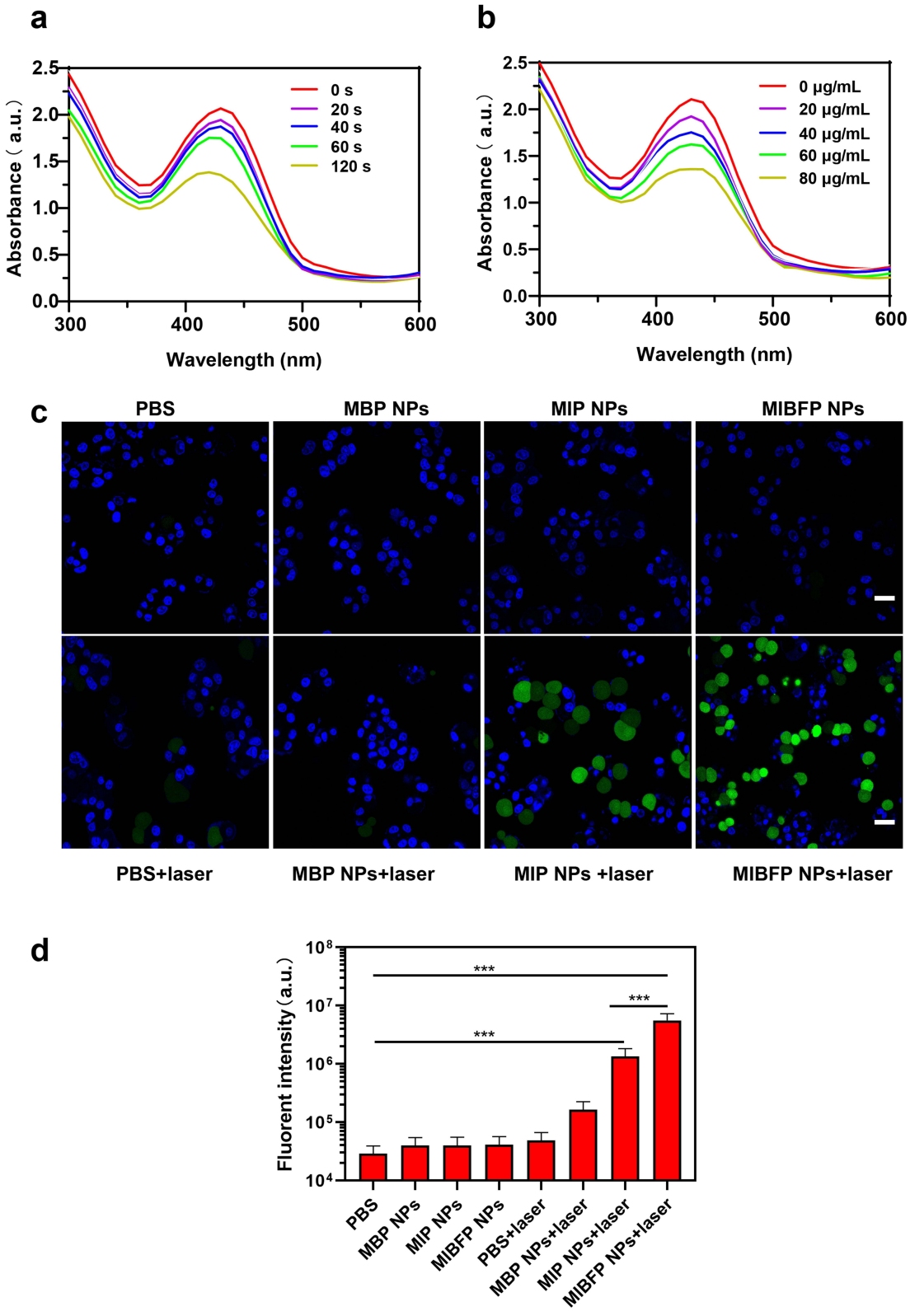

Figure 4 The intracellular ROS detection of MIBFP NPs. (**a**) Time-dependent and (**b**) Concentration-dependent ROS detection of MIBFP NPs (containing 15 μg mL^{-1} ICG) using ROS probe DPBF, whose attenuation rate at 410 nm is directly proportional to the generation rate of ROS under 808 nm laser radiation (1.0 W cm^{-2}, 2 min). (**c**) CLSM images of ZR75.1 cells dyed by DCFH-DA with various treatments. The scale bar is 25 μm. (**d**) FCM analysis of ZR75.1 cells after different treatments. (***$P < 0.001$).
Abbreviations: ROS, Reactive oxygen species; MIBFP NPs, mAbs, ICG, pB-DOX and Fe_3O_4, coloaded poly (lactic-co-glycolic acid) nanoparticles; ICG, indocyanine green; DPBF, 1.3-Diphenylisobenzofuran; CLSM, confocal laser scanning microscope; DCFH-DA, 2′,7′-dichlorofluorescin diacetate; FCM, flow cytometry; NS, no significance.

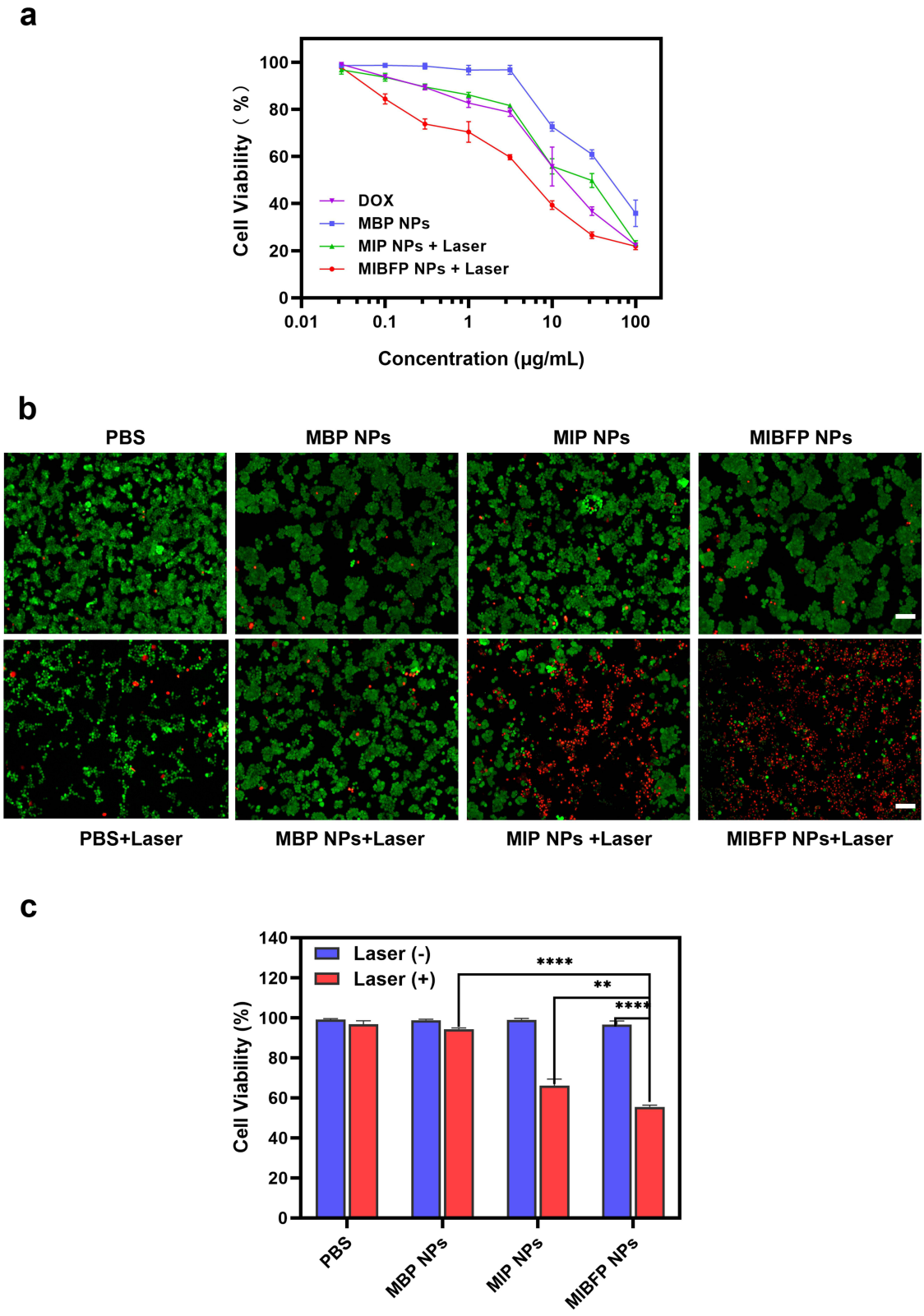

Figure 5 The cellular cytotoxicity studies of MIBFP NPs. (**a**) CCK-8 assays of DOX, MBP NPs, MIP NPs +laser and MIBFP NPs + laser in breast cancer cells ZR75.1. (**b**) FL images of live and dead ZR75.1 cells treated with PBS and different formulations after irradiation. The scale bar is 100 μm. (**c**) Cell viabilities of ZR75.1 cells after different formulations calculated using "Image J" software. (**P < 0.01, ****P < 0.0001).

Abbreviations: MIBFP NPs, mAbs, ICG, pB-DOX and Fe_3O_4, coloaded poly (lactic-co-glycolic acid) nanoparticles; FL, fluorescence; PBS, phosphate-buffered solution; NS, no significance.

The powerful and potentially dangerous functions of ROS play critical roles under many conditions that drive abnormal cell behaviour, such as cancer. Indeed, cancer cells have been shown to carry more ROS than their normal counterparts.[51] However, the consequences of these increases in ROS can be very different, with evidence that they both support and inhibit malignant behaviour. The nature of the intricacies of ROS responses in cancer argues against the simplistic approach of devising generalized therapies based on ROS regulation.[52] Cancer cells tend to carry high levels of ROS suggests that they may be more likely than normal tissue to undergo cell death in response to further oxidative stress, and indeed many current chemotherapeutic agents can function by increasing the ROS level.[53]

In this study, the ICG in the homemade targeted nanosystem will significantly increases the ROS levels by 808nm laser irradiation, PDT relies on the local generation of cytotoxic ROS to kill cancer cells, while normal tissues without light irradiation could be free from damage.[54] ROS generated by PDT could directly kill cancer cells via necrosis or apoptosis, and importantly, trigger the activation of prodrugs pB-DOX for tumor specific chemotherapy. Thus, a synergistic strategy to realize efficient co-delivery of the PS and ROS responsive prodrug but decrease the off-target toxicity of chemo drug will have great potential for cancer therapy.

In vitro and in vivo Multimodal Imaging

FL Imaging

ICG has been extensively investigated as a fluorescent contrast agent for FL imaging due to its strong optical absorption in the near-infrared region. FL imaging offers inherent advantages and provides a unique method for observing the dynamic distribution of NPs throughout the body. First, we evaluated the FL characteristics of the MIBFP NPs. To characterize their optical properties, we tested the FL intensity of the MIBFP NPs with different concentrations of ICG on orifice plates. Within the low concentration range, there was a proportional relationship between the FL intensity and ICG concentration. However, FL quenching occurred when the ICG concentration exceeded 20 μg mL^{-1} (Figure 6a). We intravenously injected MIBFP NPs into nude mice harboring ZR75.1 tumors and observed ICG FL using in vivo near-infrared imaging. By quantifying the FL intensity of ICG at different time points, we found that after 6 h of intravenous injection, the FL signal from the MIBFP NPs could be detected at the tumor site. The FL signal peaked at 12 h after injection due to the continuous accumulation of the NPs at the tumor site (Figure 6b and c). Due to the specific targeting ability of the mAbs, mice treated with MIBFP NPs still exhibited a strong FL signal at the tumor site even at 24 h post-injection. In contrast, mice treated with IBFP NPs without targeting ability exhibited widespread FL signals primarily in the liver, where the FL signals were much stronger than those in other organs; moreover, no obvious FL signals were observed in the tumors.

The tumor-bearing mice were sacrificed 24 h post-injection, and both the tumor and major organs were collected for FL imaging to confirm the tumor accumulation of the MIBFP NPs through specific mAb targeting. In vitro imaging revealed intense FL in the tumor region of mice treated with MIBFP NPs, whereas in the IBFP NP group, FL was primarily observed in the liver, with a minimal signal detected in the tumor region. The corresponding semiquantitative results (Figure 6d and e) demonstrated that the FL intensity of the MIBFP NP-treated tumors was greater than that of the IBFP NP-treated tumors.

MR Imaging

MR imaging has emerged as a widely utilized imaging modality in clinical diagnosis due to its high spatial resolution and deep tissue penetration potential. Superparamagnetic Fe_3O_4 is an optimal contrast agent for T2-weighted MR imaging. We initially validated the MR imaging performance of the MIBFP NPs at various concentrations and observed a rapid decrease in contrast to the T2-weighted MR images with increasing Fe concentration. Notably, we established a clear linear relationship between the 1/T2 value and the Fe concentration (Figure 7a), confirming the potential of the MIBFP NPs as a T2-weighted contrast agent for enhancing MRI. Motivated by the high r2 value exhibited by the MIBFP NPs in vitro, we further investigated the imaging capability of the MIBFP NPs in vivo. The imaging contrast at the tumor site gradually diminished over time and reached its maximum at 12 h post-injection (Figure 7b and c), consistent with the peak time observed during FL imaging, suggesting that peak release of Fe occurs 12 h after injection. These findings also support using this time point as an optimal time point for subsequent PDT using 808 nm laser irradiation. Due to the

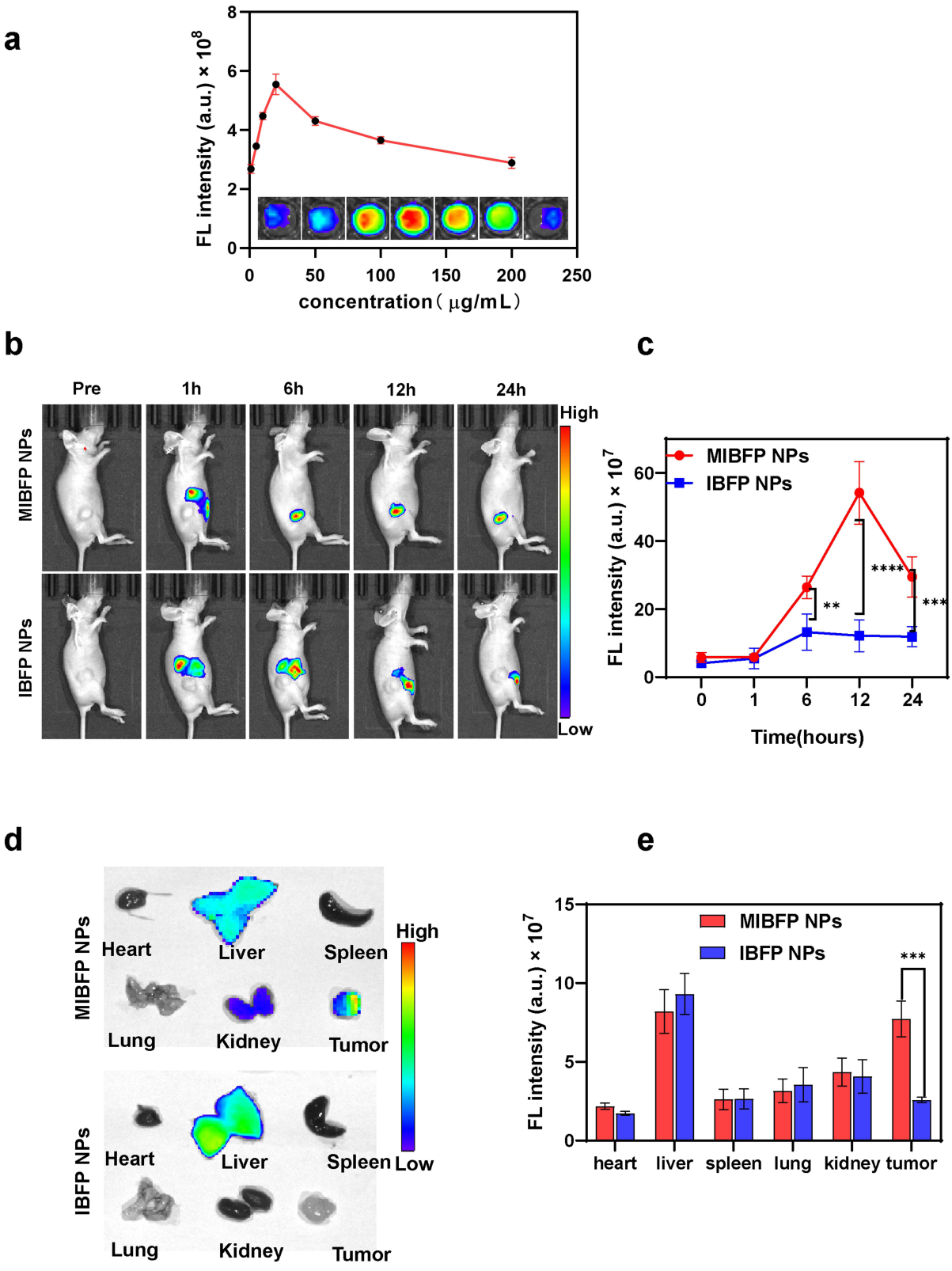

Figure 6 The FL imaging of MIBFP NPs in vitro and in vivo. (**a**) In vitro FL images and FL values of MIBFP NPs at different concentrations. (**b**) Biodistribution and FL images in vivo of ZR75.1 tumor-bearing mice after the intravenous injection of MIBFP NPs at different time points. (**c**) Changes in FL signal intensities within tumor regions at corresponding time points. (**d**) Ex vivo FL images of major organs and tumors dissected from mice 24h post injection of MIBFP NPs and (**e**) the corresponding quantitative analysis. (The data are shown as mean ± SD, n=3 per group, $^{**}P < 0.01$, $^{***}P < 0.001$, $^{****}P < 0.0001$).

Abbreviations: MIBFP NPs, mAbs, ICG, pB-DOX and Fe_3O_4, coloaded poly (lactic-co-glycolic acid) nanoparticles; FL, fluorescence; NS, no significance.

https://doi.org/10.2147/IJN.S467512 DovePress

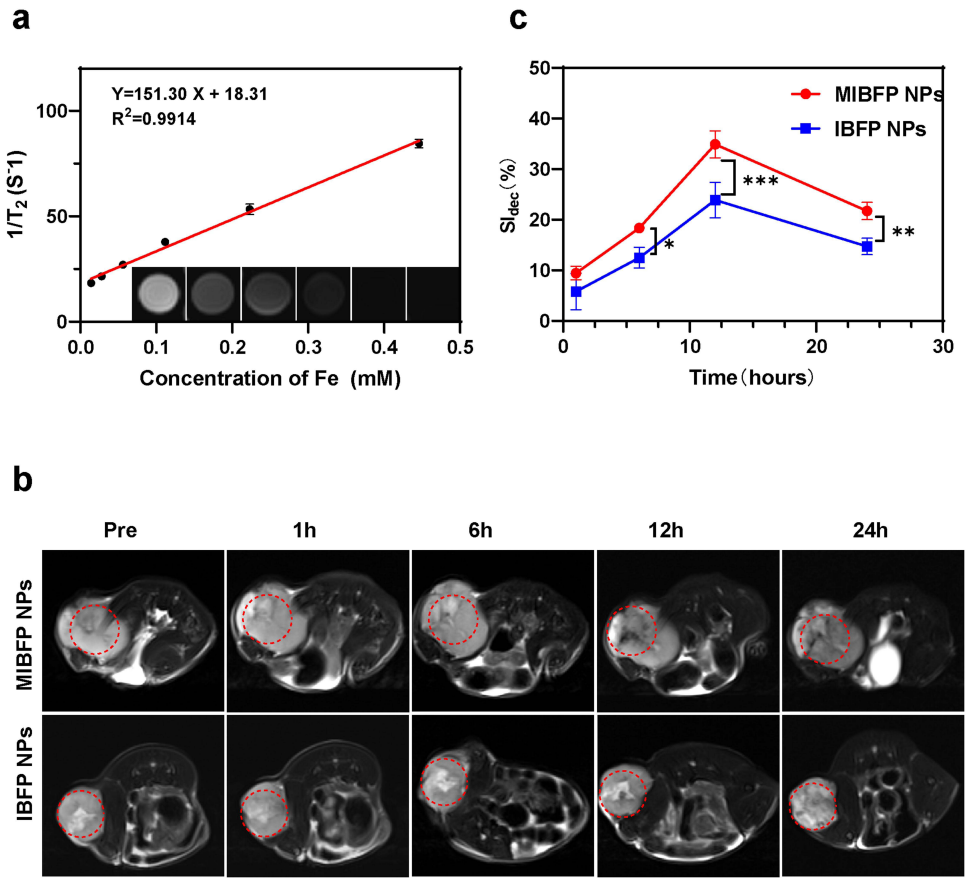

Figure 7 MR imaging assessment of MIBFP NPs in vitro and in vivo. (**a**) The curve of 1/T2 versus MIBFP NPs at elevated Fe_3O_4 concentration. Inset: T2-weighted MR intensities of MIBFP NPs at different Fe_3O_4 concentration. (**b**) MR T2 weighted Image of ZR75.1 tumor-bearing mice (region enveloped by the red dotted line) at pre, 1 h, 6 h, 12 h and 24 h post-injection of MIBFP and IBFP NPs. (**c**) Quantitative analysis of SI dec (n=3), the difference was detected in the MIBFP and IBFP NPs group. (The data are shown as mean ±SD, n=3 per group, $^*P < 0.05$, $^{**}P < 0.01$, $^{***}P < 0.001$).

Abbreviations: MIBFP NPs, mAbs, ICG, pB-DOX and Fe_3O_4, coloaded poly (lactic-co-glycolic acid) nanoparticles; MR, magnetic resonance; Fe_3O_4, superparamagnetic iron oxide; SI, signal intensity; NS, no significance.

active targeted accumulation of the MIBFP NPs at the tumor site, signal attenuation within the tumor persisted until 24 h after injection.

Thus, the in vitro and in vivo results confirmed that the MIBFP NPs not only rapidly and effectively accumulate at the tumor site but also possess T2-weighted MR imaging characteristics, facilitating accurate tumor diagnosis while guiding the selection of treatment windows and real-time monitoring during cancer therapy.

In vivo Antitumor Efficiency

The in vitro therapeutic effect of the MIBFP NPs was remarkable, and FL and MR imaging confirmed the rapid and effective accumulation of the MIBFP NPs in the tumor region, which prompted further investigation of their potential for use in in vivo therapeutics. Compared with those in the control group (Figure 8a and b), the laser-only, MIBP NP, and MIBFP NP groups exhibited negligible tumor growth inhibition. The MIBP NPs + Laser, IBFP NPs + Laser, and MIBFP NPs + Laser treatments all exhibited significant tumor inhibition, whereas no notable antitumor effect was observed in the MIP NPs + Laser group. Among these groups, the best therapeutic effect was observed in the MIBFP NPs + Laser group due to its excellent targeting ability and ability to generate ROS, indicating that therapeutic efficacy depends on NP accumulation at the tumor site. Because the prodrug pB-DOX requires stimulation by ROS for activation and transformation into toxic DOX, therapeutic efficacy is also dependent on ROS generation. Notably, compared with those in the MIBP NPs +Laser group, better therapeutic effects were achieved with Fe_3O_4-stimulated ICG-mediated ROS production in the MIBFP NPs +Laser group, synergizing PDT and chemotherapy modalities. No significant weight loss was

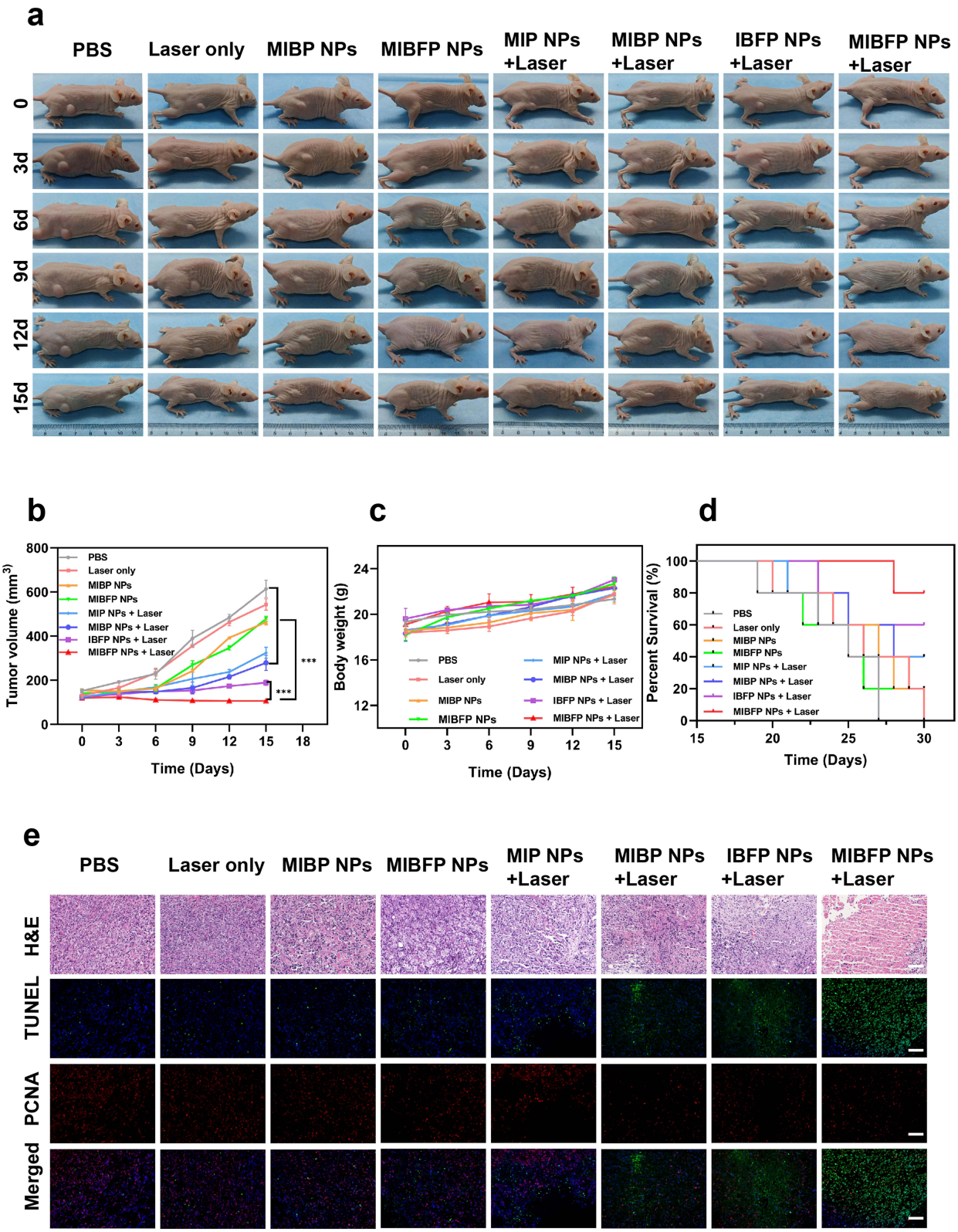

Figure 8 The combined antitumor efficiency of MIBFP NPs in vivo. (**a**) Digital photos of ZR75.1 tumor-bearing mice during the therapeutic period in vivo. (**b**) Changes in tumor volumes over 15 days after various treatments. (**c**) The body weight curves of ZR75.1 tumor-bearing mice receiving various treatments over 15 days. (**d**) Survival of different groups. (**e**) H&E, TUNEL and PCNA staining of the tumor tissue after various treatments. The Scale bars is 100 μm. (The data are shown as mean ±SD, n=5 per group, ***$P < 0.001$).

Abbreviations: MIBFP NPs, mAbs, ICG, pB-DOX and Fe_3O_4, coloaded poly (lactic-co-glycolic acid) nanoparticles; H&E, hematoxylin and eosin staining; TUNEL, Terminal-deoxynucleotidyl Transferase Mediated Nick End Labeling; PCNA, proliferating cell nuclear antigen; NS, no significance.

observed in any experimental group (Figure 8c), suggesting minimal systemic toxicity associated with the NPs or laser irradiation treatment regimens. Furthermore, the highest survival rate was recorded for mice treated with a combination of MIBFP NPs and laser irradiation (Figure 8d), providing additional evidence supporting the synergistic enhancement of PDT and chemotherapy effects mediated by MIBFP NPs.

Furthermore, the results of H&E staining and TUNEL and PCNA immunofluorescence staining (Figure 8e) further validate the synergistic enhancement of PDT and chemotherapy effects in the MIBFP NPs + Laser group. In comparison to the observations in the other groups, H&E staining revealed nuclear abnormalities, such as karyopyknosis, karyorrhexis, and karyolysis, specifically in the MIBFP NPs + Laser group. Similarly, TUNEL images revealed significant apoptosis (green FL), while PCNA images demonstrated negligible proliferation (red FL) in the MIBFP NPs + Laser group. No substantial necrosis of cardiac myocytes or myocardial fibers was observed, and there was no evidence of lesions or damage to major organs across all the experimental groups. These findings indicate that our treatment strategy effectively mitigates DOX-induced cardiotoxicity without causing significant side effects in mice (Figure S7). Overall, the MIBFP NPs exhibited potent antitumor effects with minimal systemic toxicity.

Following intravenous administration, the targeted NPs continuously accumulated at the tumor site and reached a peak concentration after 12 hours, as confirmed by FL and MRI. MIBFP NPs exhibited superior inhibitory effects on tumor growth through synergistic therapy compared to IBFP NPs. Meanwhile, the design of pB-DOX circumvents the profound cardiotoxicity associated with DOX administration, while demonstrating negligible adverse reactions in major organs. These collective endeavors have effectively mitigated the side effects of anticancer drug capsules and significantly enhanced therapeutic efficacy.

Conclusion

This study reported a mammaglobin targeting mAbs-mediated strategy to deliver ICG/pB-DOX/ Fe_3O_4/PLGA NPs by the carbodiimide approach into breast cancer under the dual-modal imaging (MR/FL) guidance. These novel antibody-targeting NPs were developed for synergistic PDT and chemotherapy of breast cancer through near-infrared laser activation. Importantly, we successfully synthesized ICG/pB-DOX/ Fe_3O_4/PLGA NPs using a double emulsion method which can combine with the mAbs targeting Mammaglobin A of breast tumor. The elaborately designed active targeting NPs achieve high tumor accumulation and significantly enhance PDT and chemotherapeutic efficiency under the dual-modal imaging guidance. Compared with the typical nanosystems for chemotherapy, the specially targeting mAbs-mediated strategy can efficiently regulate tumor cells to generate a substantial amount ROS for achieving PDT, while simultaneously triggering activation of pB-DOX for chemotherapy. The synergistic effect between PDT and chemotherapy significantly enhanced the cytotoxicity of MIBFP NPs against breast cancer. Furthermore, the FL combined MR imaging performance is conducive to monitoring the reaction of tumor sites and guiding the selection of the 808 nm laser irradiation time window during cancer therapy. Multimodal imaging integrates the advantages of individualized imaging modalities and provides more accurate biological information for the early diagnosis of tumors and monitoring of PDT and chemotherapy. In summary, MIBFP NPs represent a novel on-demand drug delivery platform that achieves exceptional antitumor potency through controlled and precise combination therapy.

Acknowledgments

Fujie Jiang and Shuling Liu contributed equally to this work.

Funding

This work has received funding by the Natural Science Foundation of Chongqing municipality (CSTB2022NSCQ-MSX1158, CSTB2023NSCQ-MSX0787, and CSTB2023NSCQ-MSX0858), the Graduate Scientific Research and Innovation Foundation of Chongqing (CYB23070 and CYS23129), Chongqing Shapingba District 2023 Technology Innovation and Application Development Project (202391), the Chongqing University Cancer Hospital Scientific Research Capacity Improvement Project (2023nlts004), and the Fundamental Research Funds for the Central Universities (2023CDJYGRH-YB04).

Disclosure

The authors report no conflicts of interest in this work.

References

1. Choi J, Shim MK, Yang S, et al. Visible-light-triggered prodrug nanoparticles combine chemotherapy and photodynamic therapy to potentiate checkpoint blockade cancer immunotherapy. *ACS Nano*. 2021;15(7):12086–12098. doi:10.1021/acsnano.1c03416
2. Yao D, Wang Y, Bian K, Zhang B, Wang D. A self-cascaded unimolecular prodrug for pH-responsive chemotherapy and tumor-detained photodynamic-immunotherapy of triple-negative breast cancer. *Biomaterials*. 2023;292:121920. doi:10.1016/j.biomaterials.2022.121920
3. Hao X, Li C, Zhang Y, et al. Programmable chemotherapy and immunotherapy against breast cancer guided by multiplexed fluorescence imaging in the second near-infrared window. *Adv Mater*. 2018;30(51):e1804437. doi:10.1002/adma.201804437
4. Shi J, Kantoff PW, Wooster R, Farokhzad OC. Cancer nanomedicine: progress, challenges and opportunities. *Nat Rev Cancer*. 2017;17(1):20–37. doi:10.1038/nrc.2016.108
5. Liu X, Xiang J, Zhu D, et al. Fusogenic reactive oxygen species triggered charge-reversal vector for effective gene delivery. *Adv Mater*. 2016;28(9):1743–1752. doi:10.1002/adma.201504288
6. Tan Y, Zhu Y, Zhao Y, et al. Mitochondrial alkaline pH-responsive drug release mediated by Celastrol loaded glycolipid-like micelles for cancer therapy. *Biomaterials*. 2018;154:169–181. doi:10.1016/j.biomaterials.2017.07.036
7. Wang S, Wang Z, Yu G, et al. Tumor-specific drug release and reactive oxygen species generation for cancer chemo/chemodynamic combination therapy. *Adv Sci*. 2019;6(5):1801986. doi:10.1002/advs.201801986
8. Lu J, Mao Y, Feng S, et al. Biomimetic smart mesoporous carbon nanozyme as a dual-GSH depletion agent and O(2) generator for enhanced photodynamic therapy. *Acta Biomater*. 2022;148:310–322. doi:10.1016/j.actbio.2022.06.001
9. Yi H, Wu J, Du Y, et al. Effect of anionic PEGylated polypeptide on gene transfection mediated by glycolipid conjugate micelles. *Mol Pharm*. 2015;12(4):1072–1083. doi:10.1021/mp500560h
10. Wang M, Zhai Y, Ye H, et al. High co-loading capacity and stimuli-responsive release based on cascade reaction of self-destructive polymer for improved chemo-photodynamic therapy. *ACS Nano*. 2019;13(6):7010–7023. doi:10.1021/acsnano.9b02096
11. Antunes F, Cadenas E. Cellular titration of apoptosis with steady state concentrations of H(2)O(2): submicromolar levels of H(2)O(2) induce apoptosis through Fenton chemistry independent of the cellular thiol state. *Free Radic Biol Med*. 2001;30(9):1008–1018. doi:10.1016/S0891-5849(01)00493-2
12. Sun C, Cao Z, Zhang X, et al. Cascade-amplifying synergistic effects of chemo-photodynamic therapy using ROS-responsive polymeric nanocarriers. *Theranostics*. 2018;8(11):2939–2953. doi:10.7150/thno.24015
13. Sun C, Wang L, Xianyu B, Li T, Gao S, Xu H. Selenoxide elimination manipulate the oxidative stress to improve the antitumor efficacy. *Biomaterials*. 2019;225:119514. doi:10.1016/j.biomaterials.2019.119514
14. Liang J, Liu B. ROS-responsive drug delivery systems. *Bioeng Transl Med*. 2016;1(3):239–251. doi:10.1002/btm2.10014
15. Li Q, Li W, Di H, et al. A photosensitive liposome with NIR light triggered doxorubicin release as a combined photodynamic-chemo therapy system. *J Control Release*. 2018;277:114–125. doi:10.1016/j.jconrel.2018.02.001
16. Wang S, Yu G, Wang Z, et al. Enhanced antitumor efficacy by a cascade of reactive oxygen species generation and drug release. *Angew Chem Int Ed Engl*. 2019;58(41):14758–14763. doi:10.1002/anie.201908997
17. Liu S, Zhang W, Chen Q, et al. Multifunctional nanozyme for multimodal imaging-guided enhanced sonodynamic therapy by regulating the tumor microenvironment. *Nanoscale*. 2021;13(33):14049–14066. doi:10.1039/D1NR01449H
18. Hao Y, Chen Y, He X, et al. Polymeric nanoparticles with ROS-responsive prodrug and platinum nanozyme for enhanced chemophotodynamic therapy of colon cancer. *Adv Sci*. 2020;7(20):2001853. doi:10.1002/advs.202001853
19. Kratz F, Warnecke A. Finding the optimal balance: challenges of improving conventional cancer chemotherapy using suitable combinations with nano-sized drug delivery systems. *J Control Release*. 2012;164(2):221–235. doi:10.1016/j.jconrel.2012.05.045
20. Ye M, Han Y, Tang J, et al. A tumor-specific cascade amplification drug release nanoparticle for overcoming multidrug resistance in cancers. *Adv Mater*. 2017;29(38). doi:10.1002/adma.201702342
21. Chen D, Zhang G, Li R, et al. Biodegradable, hydrogen peroxide, and glutathione dual responsive nanoparticles for potential programmable paclitaxel release. *J Am Chem Soc*. 2018;140(24):7373–7376. doi:10.1021/jacs.7b12025
22. Yi H, Lu W, Liu F, et al. ROS-responsive liposomes with NIR light-triggered doxorubicin release for combinatorial therapy of breast cancer. *J Nanobiotechnology*. 2021;19(1):134. doi:10.1186/s12951-021-00877-6
23. Li Q, Zhang J, Li J, et al. Glutathione-activated NO-/ROS-generation nanoparticles to modulate the tumor hypoxic microenvironment for enhancing the effect of HIFU-combined chemotherapy. *ACS Appl Mater Interfaces*. 2021;13(23):26808–26823. doi:10.1021/acsami.1c07494
24. Zhu D, Fan F, Huang C, et al. Bubble-generating polymersomes loaded with both indocyanine green and doxorubicin for effective chemotherapy combined with photothermal therapy. *Acta Biomater*. 2018;75:386–397. doi:10.1016/j.actbio.2018.05.033
25. Wang Y, Li S, Ren X, Yu S, Meng X. Nano-engineering nanomedicines with customized functions for tumor treatment applications. *J Nanobiotechnology*. 2023;21(1):250. doi:10.1186/s12951-023-01975-3
26. Dai Y, Xu C, Sun X, Chen X. Nanoparticle design strategies for enhanced anticancer therapy by exploiting the tumour microenvironment. *Chem Soc Rev*. 2017;46(12):3830–3852. doi:10.1039/C6CS00592F
27. Tian H, Zhang T, Qin S, et al. Enhancing the therapeutic efficacy of nanoparticles for cancer treatment using versatile targeted strategies. *J Hematol Oncol*. 2022;15(1):132. doi:10.1186/s13045-022-01320-5
28. Cheng Z, Li M, Dey R, Chen Y. Nanomaterials for cancer therapy: current progress and perspectives. *J Hematol Oncol*. 2021;14(1):85. doi:10.1186/s13045-021-01096-0
29. Overchuk M, Zheng G. Overcoming obstacles in the tumor microenvironment: recent advancements in nanoparticle delivery for cancer theranostics. *Biomaterials*. 2018;156:217–237. doi:10.1016/j.biomaterials.2017.10.024
30. Tafreshi NK, Enkemann SA, Bui MM, et al. A mammaglobin-A targeting agent for noninvasive detection of breast cancer metastasis in lymph nodes. *Cancer Res*. 2011;71(3):1050–1059. doi:10.1158/0008-5472.CAN-10-3091

31. Zuo L, Li L, Wang Q, Fleming TP, You S. Mammaglobin as a potential molecular target for breast cancer drug delivery. *Cancer Cell Int*. 2009;9(1):8. doi:10.1186/1475-2867-9-8
32. Narayanan K, Jaramillo A, Benshoff ND, et al. Response of established human breast tumors to vaccination with mammaglobin-A cDNA. *J Natl Cancer Inst*. 2004;96(18):1388–1396. doi:10.1093/jnci/djh261
33. Span PN, Waanders E, Manders P, et al. Mammaglobin is associated with low-grade, steroid receptor-positive breast tumors from postmenopausal patients, and has independent prognostic value for relapse-free survival time. *J Clin Oncol*. 2004;22(4):691–698. doi:10.1200/JCO.2004.01.072
34. Liu Z, Yang X, Duan C, et al. Identification and characterization of mammaglobin-A epitope in heterogenous breast cancers for enhancing tumor-targeting therapy. *Signal Transduct Target Ther*. 2020;5(1):82. doi:10.1038/s41392-020-0183-1
35. Liu F, Cheng Z, Yi H. NIR light-activatable dissolving microneedle system for melanoma ablation enabled by a combination of ROS-responsive chemotherapy and phototherapy. *J Nanobiotechnology*. 2023;21(1):61. doi:10.1186/s12951-023-01815-4
36. Li Y, Zhang P, Tang W, et al. Bright, magnetic NIR-II quantum dot probe for sensitive dual-modality imaging and intensive combination therapy of cancer. *ACS Nano*. 2022;16(5):8076–8094. doi:10.1021/acsnano.2c01153
37. Shi H, Sun Y, Yan R, et al. Magnetic semiconductor Gd-Doping CuS nanoparticles as activatable nanoprobes for bimodal imaging and targeted photothermal therapy of gastric tumors. *Nano Lett*. 2019;19(2):937–947. doi:10.1021/acs.nanolett.8b04179
38. Lee K, Lee J, Lee S, et al. MnCO3-mineralized polydopamine nanoparticles as an activatable theranostic agent for dual-modality imaging-guided photothermal therapy of cancers. *Theranostics*. 2022;12(15):6762–6778. doi:10.7150/thno.77060
39. Shi Y, Zhou M, Zhang Y, Wang Y, Cheng J. MRI-guided dual-responsive anti-tumor nanostructures for synergistic chemo-photothermal therapy and chemodynamic therapy. *Acta Biomater*. 2023;158:571–582. doi:10.1016/j.actbio.2022.12.053
40. Huang Q, Pan Y, Wang M, et al. Tumor microenvironment-responsive versatile "Trojan horse" theranostic nanoplatform for magnetic resonance imaging-guided multimodal synergistic antitumor treatment. *Acta Biomater*. 2022;147:270–286. doi:10.1016/j.actbio.2022.05.024
41. Tang Y, Chen C, Jiang B, et al. Bifidobacterium bifidum-mediated specific delivery of nanoparticles for tumor therapy. *Int J Nanomedicine*. 2021;16:4643–4659. doi:10.2147/IJN.S315650
42. Guo W, Guo C, Zheng N, Sun T, Liu S. Cs(x) WO(3) nanorods coated with polyelectrolyte multilayers as a multifunctional nanomaterial for bimodal imaging-guided photothermal/photodynamic cancer treatment. *Adv Mater*. 2017;29(4):1604157.
43. Sheng Z, Hu D, Zheng M, et al. Smart human serum albumin-indocyanine green nanoparticles generated by programmed assembly for dual-modal imaging-guided cancer synergistic phototherapy. *ACS Nano*. 2014;8(12):12310–12322. doi:10.1021/nn5062386
44. Gao S, Wang G, Qin Z, et al. Oxygen-generating hybrid nanoparticles to enhance fluorescent/photoacoustic/ultrasound imaging guided tumor photodynamic therapy. *Biomaterials*. 2017;112:324–335. doi:10.1016/j.biomaterials.2016.10.030
45. Rosenblum D, Peer D. Omics-based nanomedicine: the future of personalized oncology. *Cancer Lett*. 2014;352(1):126–136. doi:10.1016/j.canlet.2013.07.029
46. Liechty WB, Peppas NA. Expert opinion: responsive polymer nanoparticles in cancer therapy. *Eur J Pharm Biopharm*. 2012;80(2):241–246. doi:10.1016/j.ejpb.2011.08.004
47. Bertrand N, Wu J, Xu X, et al. Cancer nanotechnology: the impact of passive and active targeting in the era of modern cancer biology. *Adv Drug Deliv Rev*. 2014;66:2–25. doi:10.1016/j.addr.2013.11.009
48. Spring B, Rizvi I, Xu N, et al. The role of photodynamic therapy in overcoming cancer drug resistance. *Photochem Photobiol Sci*. 2015;14(8):1476–1491. doi:10.1039/c4pp00495g
49. Park H, Park W, Na K. Doxorubicin loaded singlet-oxygen producible polymeric micelle based on chlorine e6 conjugated pluronic F127 for overcoming drug resistance in cancer. *Biomaterials*. 2014;35(27):7963–7969. doi:10.1016/j.biomaterials.2014.05.063
50. Wang L, Sun Q, Wang X, et al. Using hollow carbon nanospheres as a light-induced free radical generator to overcome chemotherapy resistance. *J Am Chem Soc*. 2015;137(5):1947–1955. doi:10.1021/ja511560b
51. Cheung EC, Vousden KH. The role of ROS in tumour development and progression. *Nat Rev Cancer*. 2022;22(5):280–297. doi:10.1038/s41568-021-00435-0
52. Yue C, Zhang C, Alfranca G, et al. Near-infrared light triggered ROS-activated theranostic platform based on Ce6-CPT-UCNPs for simultaneous fluorescence imaging and chemo-photodynamic combined therapy. *Theranostics*. 2016;6(4):456–469. doi:10.7150/thno.14101
53. Jiang B, Zhang L, Guo X, et al. Poly(N-phenylglycine)-based nanoparticles as highly effective and targeted near-infrared photothermal therapy/photodynamic therapeutic agents for malignant melanoma. *Small*. 2017;13(8). doi:10.1002/smll.201602496
54. Liu W, Wang Y, Li Y, et al. Fluorescent imaging-guided chemotherapy-and-photodynamic dual therapy with nanoscale porphyrin metal-organic framework. *Small*. 2017;13(17):1603459.